Epitaxial stabilization of the perovskite phase in $(Sr_{1-x}Ba_x)MnO_3$ thin films

*Eric Langenberg[1, †, *], Roger Guzmán[2], Laura Maurel[1,3], Lourdes Martínez de Baños[1], Luis Morellón[1,3], M. Ricardo Ibarra[1,2,3], Javier Herrero-Martín[4], Javier Blasco[3,5], César Magén[2,3,6], Pedro A. Algarabel[3,5], José A. Pardo[1,2,7].*

[1]Instituto de Nanociencia de Aragón, Universidad de Zaragoza, 50018 Zaragoza, Spain.

[2]Laboratorio de Microscopías Avanzadas, Instituto de Nanociencia de Aragón, Universidad de Zaragoza, 50018 Zaragoza, Spain.

[3]Departamento de Física de la Materia Condensada, Universidad de Zaragoza, 50009 Zaragoza, Spain.

[4]ALBA Synchrotron, 08290 Cerdanyola del Vallès, Barcelona, Spain.

[5]Instituto de Ciencia de Materiales de Aragón, Universidad de Zaragoza-CSIC, 50009 Zaragoza, Spain.

[6]Fundación ARAID, 50018 Zaragoza, Spain.

[7]Departamento de Ciencia y Tecnología de Materiales y Fluidos, Universidad de Zaragoza, 50018 Zaragoza, Spain.

ABSTRACT: A novel mechanism of ferroelectricity driven by off-centering magnetic Mn^{4+} ions was proposed in $(Sr_{1-x}Ba_x)MnO_3$, in its ideal perovskite phase, which yields enormous expectations in the search for strong magnetoelectric materials. Still, the desired perovskite phase has never been stabilized in thin films due to its extremely metastable character. Here, we report on a thorough study of the perovskite phase stabilization of $(Sr_{1-x}Ba_x)MnO_3$ thin films, $0.2 \leq x \leq 0.5$, grown by pulsed laser deposition onto (001)-oriented perovskite substrates. X-ray diffraction measurements and scanning transmission electron microscopy reveal that, under appropriate deposition conditions, the perovskite phase is fully stabilized over the non-ferroelectric hexagonal phase, despite the latter being increasingly favored on increasing Ba-content. Moreover, we have managed to grow epitaxial coherent cube-on-cube $(Sr_{1-x}Ba_x)MnO_3$ films upon strains ranging from 0% to 4%. Our results become a milestone in further studying perovskite $(Sr_{1-x}Ba_x)MnO_3$ thin films and pave the way for tailoring ferroic and magnetoelectric properties either by strain engineering or Ba-doping.

KEYWORDS: $(Sr_{1-x}Ba_x)MnO_3$ thin films, perovskite phase stability, epitaxial stabilization, ferroelectrics, multiferroics, pulsed laser deposition

INTRODUCTION

Controlling the magnetic state of materials by an electric field –instead of the conventional use of the conjugated magnetic field– would yield enormous benefits in technological applications where solutions based on magnetoelectric effects have been proposed, such as the design of high-density non-volatile magnetic memories.[1–4] For this purpose, multiferroic materials in which ferroelectric and magnetic order coexist in the same phase inherently lie in an excellent position to show strong magnetoelectric coupling. Apart from the practical interest, understanding the interplay between electric polarization and magnetism in solids, which is still in its infancy, makes these materials very appealing in terms of fundamental research.

Many ferroelectric materials so far identified are oxides with perovskite structure (ABO_3) in which the required non-centrosymmetric structure is achieved by the off-centering of d^0-B cations, *i.e.* with no electrons at the *d*-orbitals.[2,3] This d^0 condition was argued to favor the polar instability by softening the electrostatic repulsion of the surrounding O^{2-} ions together with the strong B – O covalent bond.[5] Instead, magnetic perovskites contain magnetic cations at the B-site, *i.e.* with partially filled *d* shells, giving rise to the common exclusion between ferroelectricity and magnetism.[1–3,6] This fact has promoted an intense research on new mechanisms of ferroelectricity in the last decade, like charge ordering,[7] geometrical ferroelectricity,[8] the stereochemical activity of lone-pair electrons of Bi^{3+} and Pb^{2+} cations,[9,10] or ferroelectricity induced by unconventional spin order.[11] However, common to all these multiferroic materials is the fact that either they have strong ferroic properties, but then very weak coupling between them or, conversely, they do show very strong magnetoelectric coupling, but very low polarization values and/or Curie temperatures.

The occurrence of ferroelectricity in alkaline-earth manganites was recently proposed theoretically,[12–15] provided that the unit cell lattice is large enough to minimize the electrostatic repulsion of oxygens in MnO_6 octahedra, and thus promoting Mn off-centering. This may be achieved by using increasingly larger A-size cations (Ba^{2+}> Sr^{2+}> Ca^{2+}), enhancing the so-called chemical pressure. Indeed, this was experimentally confirmed by partially replacing Sr with Ba in bulk $(Sr_{1-x}Ba_x)MnO_3$ for x > 0.4.[16,17] Remarkably enough, in this case the polar state is driven by the off-centering of non-d^0 magnetic cation (Mn^{4+}, d^3), a mechanism never found before. Moreover, significant polarization values (tens of $\mu C/cm^2$) and ferroelectric ordering above room temperature (~400 K) were found,[16,17] rivaling those of conventional ferroelectrics. Commensurate G-type antiferromagnetic order –arisen from Mn – O – Mn superexchange interaction– develops below 230 K for x = 0, gradually decreasing the Néel temperature (T_N) on increasing Ba-content (T_N = 185 K for x = 0.5). [16,17] As the same cation, Mn^{4+}, is responsible for both ferroelectric and magnetic order,[17,18] very strong magnetoelectric coupling is expected: magnetic superexchange interaction promotes Mn – O – Mn ions to be aligned (bond angle close to 180º), whereas ferroelectric distortion prompts Mn off-centering, thus decreasing the bond angle.[19] Moreover, the strong dependence of the polar phonon on spin order in these alkaline-earth manganites[15,20] could also be used to tune the magnetic phase by an electric field, *i.e.* from antiferromagnetic to ferromagnetic order, which can be achieved by relatively small electric fields.[21]

Here, we focus on $(Sr_{1-x}Ba_x)MnO_3$ thin films. High Ba-content is required to develop a ferroelectric phase. However, the perovskite phase is destabilized by continuously increasing the size of the A-cation (increasing Ba-content), as it cannot be accommodated in the cubic structure.[12,22–24] Indeed, different non-ferroelectric hexagonal polymorphs are the ground state of

the $(Sr_{1-x}Ba_x)MnO_3$ solid solution,[22,25] as their face-sharing BO_6 octahedra network provides larger size cavities for A-cations.[23] The perovskite stability can be semi-quantitatively described by the Goldsmith tolerance factor:

$$t = \frac{r_A + r_O}{\sqrt{2} \cdot (r_B + r_O)} \quad (1)$$

where r_A, r_B and r_O denote the ionic radii of A, B and oxygen ions, respectively. An ideal cubic perovskite is obtained for $t \sim 1$ (<A–O> and $\sqrt{2}$·<B–O> bond lengths are similar), whereas for $t > 1$ the hexagonal phase prevails. In $(Sr_{1-x}Ba_x)MnO_3$ system t becomes significantly larger than the unity on increasing Ba-content ($1.04 \leq t \leq 1.08$ for $0 \leq x \leq 0.6$). Hence, difficulty in these compounds lies in the stabilization of the extreme metastable perovskite phase, as increasing Ba content gives rise to large t values. Note that bulk $(Sr_{1-x}Ba_x)MnO_3$ perovskite phase is only stable for $x < 0.15$ at temperatures higher than 1400°C.[22] The perovskite structure for higher Ba-doping values was only obtained under high hydrostatic pressures (~6.5 GPa).[16] To date, Ba-doped $SrMnO_3$ has never been synthesized in its perovskite phase in thin films, even for relatively low values of doping ($x \sim 0.2$). It is clear that practical applications (*e. g.* multilayer heterostructures) require a stable perovskite phase in thin film form. Apart from device implementation, strain engineering by epitaxial growth of thin films on a substrate gives an additional degree of freedom, absent in bulk specimens, which can be used to gain access to novel phases and thus engineer new or enhanced functional properties.[26] Bulk cubic perovskite $(Sr_{1-x}Ba_x)MnO_3$ solid solution becomes tetragonal above $x > 0.4$ due to the onset of the ferroelectric order.[16] Instead, by appropriate selection of the substrates this tetragonal distortion could be imposed for lower values of Ba-content as long as epitaxially strained $(Sr_{1-x}Ba_x)MnO_3$ films are grown (*i.e.* the in-plane lattice parameters replicate those of the substrate). In fact, non-polar bulk $SrMnO_3$ is

predicted to become ferroelectric in epitaxial strained thin films under 1% tensile strain (in-plane tetragonal distorted)[14] and indeed we have recently demonstrated that 1.7%-strained $SrMnO_3$ thin films are polar.[27] For the sake of simplicity, the term pseudocubic will refer hereinafter to the perovskite phase of $(Sr_{1-x}Ba_x)MnO_3$ (in contrast to the hexagonal phase) either in its cubic or tetragonally distorted form.

In this work, we report for the first time the synthesis of high crystal quality epitaxial thin films of the perovskite phase of $(Sr_{1-x}Ba_x)MnO_3$ solid solution for Ba content ranging $0.2 \leq x \leq 0.5$. In bulk, high hydrostatic pressures are used for synthesizing the metastable pseudocubic phase.[16] Here, instead, we use an alternative powerful mechanism for films, the so-called epitaxial stabilization,[28] and widely used for metastable phase stabilization,[29–31] which consists of utilizing underlying substrates that structurally resembles the phase that is to be formed in the film (in our case perovskite substrates). In this manner, the interface energy, lower for the pseudocubic phase than for the hexagonal one, favors the formation of crystallographic nucleus in the perovskite phase during the deposition process and thus promotes the pseudomorphic film growth with regard to the substrate. Still, we demonstrate that stability of the perovskite phase, which declines on increasing Ba content, is only found in a very delicate balance of growth conditions.

EXPERIMENTAL SECTION

$(Sr_{1-x}Ba_x)MnO_3$, $0.2 \leq x \leq 0.5$, thin films were grown by pulsed laser deposition (PLD) onto several commercially-available perovskite substrates, namely, $YAlO_3$ (YAO), $LaAlO_3$ (LAO), $(LaAlO_3)_{0.3}$-$(Sr_2AlTaO_6)_{0.7}$ (LSAT), $SrTiO_3$ (STO), $DyScO_3$ (DSO), $TbScO_3$ (TSO) and $GdScO_3$ (GSO), having an average pseudocubic lattice parameter ranging from 3.70 Å (YAO) to 3.97 Å (GSO). All the substrates used are (001)-oriented –assuming a pseudocubic lattice.[32,33] The

variety of substrate lattice parameters spans a wide range of in-plane misfit strain: from compressive -4% to tensile +4%, depending on the Ba-content. For the sake of clarity, given the number of substrates and Ba compositions a sketch showing their lattice parameters is depicted in Figure 1. Stoichiometric polycrystalline $(Sr_{1-x}Ba_x)MnO_3$ ceramics with single-phase hexagonal 4H structure were prepared by solid state reaction using as primary reactants $SrCO_3$, $BaCO_3$ and $MnCO_3$ [see Supporting Information] and used as targets for the PLD growth. Laser fluence and repetition rate were set at ~1 J/cm^2 and 10 Hz, respectively. A wide range of substrate temperatures and oxygen pressures was explored in the growth process, setting values ranging 700-1000°C and between 10^{-5} Torr and 10^{-1} Torr, respectively. It is worth noting that temperature is not measured from the substrate directly but with a thermocouple embedded in the heater, so that the actual temperature is slightly lower than the nominal one. After deposition the films were cooled down at 10°C/min in a pure oxygen atmosphere (700 Torr). Selected films were in-situ annealed at different temperatures for 1 h at 700 Torr of oxygen pressure. Film thickness, measured by X-ray reflectivity, was varied between 5 and 50 nm.

The pseudocubic phase stability was ex-situ monitored by recording θ/2θ X-ray diffraction (XRD) patterns of the films around the hypothetical 2θ position of the pseudocubic (002) reflection of $(Sr_{1-x}Ba_x)MnO_3$ compound, according to bulk pseudocubic lattice parameters.[16] Long-range θ/2θ scans were performed in order to detect any parasitic phase in the films. The structure, crystal quality and epitaxial coherence of the films were evaluated by XRD reciprocal space maps (RSM), XRD rocking curves and high angle annular dark field scanning transmission electron microscopy (HAADF-STEM). HAADF-STEM analyses were carried out in a FEI Titan 60–300 microscope operated at 300 kV, fitted with a high-brightness field emission gun (X-FEG) and a CETCORCs probe corrector from CEOS to provide a spatial resolution below 1 Å in

STEM mode. Cross-section TEM specimens were prepared by tripod mechanical polishing and low-voltage Ar^+ ion milling.

Soft X-ray absorption spectroscopy (XAS) measurements at the Mn $L_{2,3}$ and O K edges were performed on the BL29-BOREAS beamline at the ALBA Synchrotron (Barcelona, Spain). Data were recorded at room temperature by means of surface-sensitive total electron yield. MnO was simultaneously measured as an energy calibration reference. The nominal flux on the BL29-BOREAS beamline was on the order of 10^{12} photons/s with an energy resolution $\Delta E/E \sim 10^{-4}$. In order to avoid a possible photoreduction of Mn ions, photon flux and exposure time were controlled.

RESULTS AND DISCUSSION

A. Perovskite phase stability

Figure 2a-d shows the θ/2θ XRD patterns –around the pseudocubic (002) reflection of the substrate– of $(Sr_{1-x}Ba_x)MnO_3$ films grown at different illustrative oxygen pressures on selected substrates, while fixing the substrate temperature at 1000°C. At low oxygen pressures, apart from the substrate reflection, an additional XRD peak clearly appears in the 2θ region where pseudocubic (002) reflection of $(Sr_{1-x}Ba_x)MnO_3$ is expected. Moreover, long-range θ/2θ XRD (not shown) and STEM images of cross sections of these samples (illustratively, Figure 3 shows that of $Sr_{0.6}Ba_{0.4}MnO_3$ film grown on TSO) evidence that the films are pure pseudocubic with no secondary phases, so that these additional XRD reflections in Figure 2a-d unequivocally correspond to the perovskite phase. It is worth noting the presence of interference fringes (Laue oscillations) of the (002) Bragg diffraction peak of the film, which indicates high crystal quality and crystalline coherence along the film thickness. The crystal quality of the films is corroborated by the rocking curves of the (002) reflection (see for instance Figure 4 for the film

with 20% Ba grown on LSAT), in which the full width at half-maximum (FWHM) is found to be smaller than 0.02° (Figure 4b) for all the fabricated pseudocubic $(Sr_{1-x}Ba_x)MnO_3$ films, though broader than the (002) reflection of the single-crystal substrates (Figure 4c). Yet it is worth remarking that these FWHM values are extremely small, showing the same crystal quality (or even enhanced) compared to most common perovskite oxide thin films.[34-37] RSM around the (103) Bragg reflection of these $(Sr_{1-x}Ba_x)MnO_3$ films are shown in Figure 5. In each Ba composition the in-plane component ($Q_{parallel}$) of the scattering vector $\boldsymbol{Q}$ is coincident with that of the substrate (indicated by guide-to-eye dotted line), which indicates that the in-plane lattice parameters of perovskite $(Sr_{1-x}Ba_x)MnO_3$ films adopt those of the substrates ($a_{film} = a_{substrate}$), confirming the epitaxial coherent growth (i.e. fully strained) and the pseudocubic structure. Further analysis of the structure of strained perovskite $(Sr_{1-x}Ba_x)MnO_3$ films is discussed in Sect. B. Importantly enough, we demonstrate for the first time the feasibility to obtain the perovskite phase in $(Sr_{1-x}Ba_x)MnO_3$ films through epitaxial stabilization combined with the use of sufficiently low oxygen pressure.

However, at intermediate oxygen pressures, the film (002) Bragg peak monotonously broadens and Laue oscillations are increasingly damped, clearly indicating a deterioration of the crystal quality of the film (Figure 2a-d). Eventually, at even higher oxygen pressures, the pseudocubic reflection disappears, which points to the perovskite phase being barely present in the best-case scenario. In reality, STEM images of the films grown at high pressures (Figure 6) reveal a scenario, in which the crystal quality is lost and the epitaxial coherence is destabilized. We shall come back to a deeper phase analysis later on. Remarkably enough, this oxygen-pressure dependence of the perovskite phase stabilization of $(Sr_{1-x}Ba_x)MnO_3$ is strongly Ba-dependent. Whereas for low Ba-content ($x \sim 0.2$) high-crystal-quality pseudocubic phase is found up to

relatively high pressures (~$5 \cdot 10^{-2}$ Torr), above x ~ 0.3 an abrupt change is observed, in which lowering the oxygen pressure by three orders of magnitude (~10^{-5} Torr) is required to obtain pure pseudocubic films, as we depict in Figure 7 (note that we have included our previous results in non-doped $SrMnO_3$ thin films).[27]

The extremely low oxygen pressure needed for the synthesis of the pseudocubic phase (especially for large Ba-contents) suggests that the formation of oxygen vacancies ($V_O^{\bullet\bullet}$) during thin film growth plays a central role in its stability. Any $V_O^{\bullet\bullet}$ (charge +2) is to be compensated by opposite charge defects in order to retain charge neutrality in the compound, *i.e.* replacing two Mn^{4+} with two Mn^{3+}. The fact that the pseudocubic phase is obtained for low oxygen pressures (Figure 2) can be explained by the larger size of Mn^{3+} ions with regard to that of Mn^{4+} (0.645 Å and 0.530 Å in octahedral coordination, respectively),[38] which counteracts the effect of the use of large cations (Ba^{2+}) at the A-site and approaches the ideal cubic perovskite tolerance factor (Eq. 1). Thus, it is clear that on increasing Ba-content, the presence of more Mn^{3+} ions is required during synthesis, forcing the use of continuously lower oxygen pressures (as shown in Figure 7). Yet it is worth noting that this relation between oxygen pressure and Ba-content shows an abrupt drop above x ~ 0.3 (Figure 7). This is probably reflecting a strong increase of the instability of the perovskite phase above 30% Ba-content. Controlling the presence of $V_O^{\bullet\bullet}$ during thin film deposition provides, hence, a determinant mechanism to stabilize the pseudocubic phase in $(Sr_{1-x}Ba_x)MnO_3$ thin films. Additionally, low oxygen pressures increase the energy of the ablated species arriving to the substrate from the target, which could be particularly important when very high substrate temperatures are required for well-ordered crystal growth as we will discuss later on.

Because of the deliberate formation of $V_O^{\bullet\bullet}$ during thin film synthesis, after growth films are slowly cooled down, *in-situ*, in a pure O_2 atmosphere (700 Torr) in order to completely oxygenate them. It is worth mentioning that in bulk these perovskites can be completely oxidized by annealing in air for a short time (few minutes) at low temperatures (< 500°C).[22,23]

In order to assess the temperature dependence of the pseudocubic phase stability, $(Sr_{1-x}Ba_x)MnO_3$ thin films were grown at different temperatures but fixed O_2 pressure, namely, $5\cdot10^{-2}$ Torr for x = 0.2 and $5\cdot10^{-5}$ Torr for x = 0.3, 0.4, 0.5. Note that at those oxygen pressures pure pseudocubic films are obtained when grown at 1000°C (Figure 2a-d). Illustratively, this temperature dependency is shown in Figure 8a corresponding to the θ/2θ XRD patterns of $(Sr_{0.7}Ba_{0.3})MnO_3$ films on TSO, but the same trend is found for the rest of Ba-content films (not shown): at 700°C and below, no clear XRD reflection is observed, but rather a broad amorphous peak. It is worth remarking that this temperature tends to be high enough for the synthesis, by PLD and related techniques, of most of the common perovskite oxide films.[2] However, it appears to be insufficient for the pseudocubic phase stabilization of $(Sr_{1-x}Ba_x)MnO_3$, probably due to its strong metastable character. It might be enlightening the fact that the stabilization of the perovskite phase over the hexagonal one in bulk $(Sr_{1-x}Ba_x)MnO_3$ for x < 0.15 at atmospheric pressure also requires very high synthesis temperature (above 1400°C for x = 0).[22] In similar systems in which the cubic and the hexagonal phase compete with each other, like bulk $Ba_{0.5}Sr_{0.5}(Co_{0.8}Fe_{0.2})O_3$, the hexagonal one is also reported to be favored below a certain temperature threshold (≤ 840°C).[39] On increasing temperature the (002) XRD peak of the films gradually becomes defined, signaling the gradual formation of the perovskite phase. Above 900°C pseudocubic films with high crystal quality are obtained as proved by the Laue oscillations and rocking curves (Figure 8 b-e).

Next we assess the pseudocubic phase stability along the films thickness. Figure 9 shows the θ/2θ XRD patterns of $(Sr_{0.6}Ba_{0.4})MnO_3$ thin films of different thickness grown at the optimal deposition conditions (1000°C and $5 \cdot 10^{-5}$ Torr oxygen pressure). As can be seen, on increasing thickness the film (002) XRD reflection asymmetrically broadens (toward larger 2θ values), indicating a gradual deterioration of the pseudocubic phase and the presence of secondary crystal structures. Identical behavior is found in films with other Ba contents (not shown), in which the pseudocubic phase is destabilized above a critical thickness, t_{max}. A careful structural analysis of these films has been carried out on HAADF-STEM images of cross section specimens of 50-nm-thick $(Sr_{0.6}Ba_{0.4})MnO_3$ cut along [110] planes of the substrate (Figure 10). Figure 10a unveils a complex twinned structure comprising sets of twin boundaries (TB) forming a ~55°-angle with respect to the substrate-film interface (Figure 10b), thus following the <111> direction (note that <110> and <111> directions forms an angle close to that value). A close inspection (Figure 10b-c) reveals a tetragonal twinning where large epitaxially-oriented twin domains –those following the epitaxial relationship with the substrate, *i.e.* $[110]Sr_{0.6}Ba_{0.4}MnO_3(001)//[110]_{pc}TSO(001)_{pc}$– and misoriented twin domains are separated by {111} TB planes, sketched as blue and green in Figure 10d, respectively. Misoriented domains are much thinner, being their average thickness of about few unit cells (Figure 10b-c), and strongly tilted respect to [001] growth direction. These domains seem to nucleate above a critical thickness (Figure 10a), giving support to the previous XRD results. Importantly enough, not all twin domains are pseudocubic. According to Fast Fourier Transforms (FFT) obtained from regions between different twin domains (Figure 11a), not only the perovskite phase is found (Figure 11b) but also the hexagonal one (Figure 11c), evidencing the aforementioned scenario of competing phases.

Although an accurate value of this critical thickness, t_{max}, was not determined, it was roughly estimated by analyzing above which thickness the (002) XRD reflection of the films begins to deteriorate as shown in Figure 9. For this purpose θ/2θ XRD scans (not shown) were performed on a wide thickness range of $(Sr_{1-x}Ba_x)MnO_3$ thin films grown on STO for x = 0.2 and on DSO for x = 0.3, 0.4, 0.5, displaying 1.92%, 2.76%, 2,44% and 2.11% of mismatch, respectively. Remarkably enough, t_{max} monotonously decreases upon Ba-doping (Figure 12) due to the increasingly metastable character of the perovskite phase on increasing the Ba-content. Thus, the effect of the perovskite substrate (epitaxial stabilization) to induce the pseudocubic phase in $(Sr_{1-x}Ba_x)MnO_3$ is lost in a few nanometers of thickness (especially for Ba-rich films), signaling the difficulty to obtain thick films of these compounds as suggested previously.[12]

The aforementioned scenario is experimentally found when the films are grown either with excessive oxygen pressure or above the critical thickness (both criteria being Ba-dependent), the former because the oxygen pressure is being increased and thus favoring the more stable hexagonal phase and the latter because the film is becoming thick enough to inhibit the epitaxial effect of the substrate on inducing the pseudocubic phase in the film. Not surprisingly this correlates with XRD results showing the pseudocubic reflection being damped. Driven by the competition between the stable hexagonal phase and the epitaxially induced pseudocubic phase, we argue that the formation of this twin domain system along the pseudocubic [111] direction must correspond to a mechanism of "phase relaxation" of the highly-metastable perovskite phase.

Finally, we analyze the effect of the epitaxial strain on the pseudocubic phase stability of $(Sr_{1-x}Ba_x)MnO_3$ films. Figure 13 shows the θ/2θ diffractograms of $(Sr_{0.6}Ba_{0.4})MnO_3$ thin films grown at the optimal deposition conditions (1000°C and $5 \cdot 10^{-5}$ Torr) and with similar thickness

(between 10 and 12 nm) on different substrates, covering a wide range of epitaxial strain values. For tensile strains (DSO, TSO and GSO) the pseudocubic (002) reflection of $(Sr_{0.6}Ba_{0.4})MnO_3$ film appears clearly defined, evidencing that the perovskite phase is completely stabilized. It should be remarked that these films are fully strained (not shown). For films weakly strained, *i.e.* close to 0% (STO and LSAT), the pseudocubic phase is also stabilized. However, for compressive strain (YAO and LAO) the film pseudocubic (002) reflection is barely present, pointing out the poor crystal quality of the perovskite phase or its presence is strongly diminished. Regardless the oxygen pressure during growth, identical trends are found for the rest of Ba-doped films (not shown): the perovskite phase is not stabilized on moderately compressive substrates. This behavior may be related to the fact that compressive strain hinders the stabilization of oxygen vacancies in the film structure during synthesis as the consequent replacement of Mn^{4+} with Mn^{3+} is accompanied by an increase of the film unit cell volume which cannot be accommodated in small-lattice-parameter substrates, *i.e.* due to the increased energy associated to the epitaxial elastic deformation.

B. Structure of strained perovskite $(Sr_{1-x}Ba_x)MnO_3$ films

In this section we take a deeper insight into the structure of the pseudocubic $(Sr_{1-x}Ba_x)MnO_3$ films grown at the optimal deposition conditions. For this purpose RSM were recorded. Illustratively, RSM around (103) Bragg reflection of $(Sr_{1-x}Ba_x)MnO_3$ films are shown in Figure 5. As observed, in each Ba composition the films are fully strained (as proved by $Q_{parallel}$ being coincident with that of the substrate). The same results are found for the pseudocubic films grown on the rest of tensile strained substrates (not shown). Taking into account that (103) reflection is used, for a perfect cubic unit cell of $(Sr_{1-x}Ba_x)MnO_3$ films the out-of-plane component (Q_{perp}) of the film reciprocal space vector should equal three times $Q_{parallel}$, which is

not the case. Thus, the unit cell of $(Sr_{1-x}Ba_x)MnO_3$ films adopt a tetragonal structure.[32] As aforementioned, note that bulk $(Sr_{1-x}Ba_x)MnO_3$, in the perovskite phase, is cubic for $x \leq 0.4$ and becomes tetragonal above that Ba-doping value due to the development of a polar phase.[16] Here, however, the epitaxial strain exerted by the substrate forces $(Sr_{1-x}Ba_x)MnO_3$ unit cell to be tetragonal even for $x \leq 0.4$.

For the same substrate, Q_{perp} of the film is Ba-dependent (not shown): it decreases on increasing Ba-content. This reflects that the out-of-plane lattice parameter of $(Sr_{1-x}Ba_x)MnO_3$ films increases upon Ba-doping due to the larger ionic size of Ba^{2+} compared to Sr^{2+}.[38] On the other hand, by fixing the Ba-content and increasing the tensile strain through the substrate choice, Q_{perp} increases, indicating that the out-of-plane lattice parameter of $(Sr_{1-x}Ba_x)MnO_3$ films diminishes upon tensile strain, due to the material's elastic deformation. This behavior is illustratively shown in Figure 14 for 20% Ba-doped films, yet the same trend is found for the rest of Ba compositions. Therefore, the unit cell lattice parameters of $(Sr,Ba)MnO_3$ system can be modified at will either by strain or by Ba-doping as shown in Figure 15a.[40] For comparison we have included the bulk values (open symbols).[16] It is worth noting that the magnitude of the controlled modification of the structure of strained $(Sr_{1-x}Ba_x)MnO_3$ films is huge and radically overcome the possibilities of bulk specimens, which represent a small region in the diagram out-of-plane vs in-plane lattice parameter (Figure 15a). Moreover, we can significantly increase the magnitude of the tetragonality (defined as c/a, where c and a denote the out-of-plane and in-plane lattice parameter, respectively), apart from changing from $c/a > 1$ to $c/a < 1$, which is not possible in bulk. This provides access to novel phases absent in bulk specimens and gives a huge versatility when it comes to designing or tuning functional properties such as ferroic transition temperatures, polar phases, polar axis, magnetic ground states or magnetoelectric coupling since

all those properties are intimately related to the expansion/contraction of the lattice parameters of the alkaline-earth manganites.[12–16,19–21]

Interestingly enough, the unit cell volume of $(Sr_{1-x}Ba_x)MnO_3$ films is noticeably larger than that of the bulk (Figure 15b). Additionally, it is strain dependent *i.e.* it increases upon tensile strain (or, equivalently, on increasing the in-plane lattice parameter as shown in Figure 15b). This is related to the fact that the unit cell volume of the strained film only preserves that of the bulk when Poisson coefficient equals 0.5, which is rarely found in manganites.[41–43] Furthermore, it was predicted by first-principles calculations in the parent compound $CaMnO_3$ that tensile strain may also be accommodated by creating oxygen vacancies due to the replacement of Mn^{4+} with larger Mn^{3+}, instead of the conventional enlargement of the intrinsic bulk unit cell lattice parameters.[44] Consequently, $CaMnO_3$ unit cell volume was proposed to significantly increase when tensile strain is increased.[44] Our experimental results in $(Sr_{1-x}Ba_x)MnO_3$ films reflect a similar strain accommodation mechanism. Taking into account that these manganites are quickly oxygenated at low temperatures,[22,23] several annealings at different temperatures and full oxygen atmosphere (700 Torr) were performed in-situ immediately after growth. The θ/2θ diffractograms of the different annealings (not shown) reveal that the 2θ position of the (002) film reflection remains unaltered at any event, which means that the structure of the film is independent of the annealing under an oxidizing atmosphere. Irrespective of the annealing process, it is worth remarking that all the films were cooled down at full oxygen atmosphere (700 Torr) at low rate (-10ºC/min), so they are expected to be completely oxidized. Thus, either the previously suggested strain-mediated oxygen vacancies are structurally clamped due to the more stable $(Sr_{1-x}Ba_x)Mn^{4+}_{1-2\delta}Mn^{3+}_{2\delta}O_{3-\delta}$ phase under tensile strain or $(Sr_{1-x}Ba_x)MnO_3$ films are actually oxygenated and the strain-dependence of the unit cell volume arises from deviation of

Poisson's ratio from ideal 0.5 value. In order to shed some light on the valence of Mn, XAS spectrum at the Mn $L_{2,3}$ edges (probing $2p \rightarrow 3d$ transitions) were recorded on strained $Sr_{0.5}Ba_{0.5}MnO_3$ film grown on GSO substrate (shown in Figure 16a). This technique is very sensitive to the electronic state and local environment of the photo-absorber atom and we have compared our measurement to the Mn $L_{2,3}$ spectra of $LaMnO_3$ and $CaMnO_3$ reference samples,[45] in which Mn oxidation state is clearly 3+ and 4+, respectively. Direct comparison of XAS spectra in Figure 16a evidence similar features for $CaMnO_3$ reference sample and $Sr_{0.5}Ba_{0.5}MnO_3$ film, in opposition to the spectrum collected from $LaMnO_3$ reference sample. Hence, this result strongly supports the occurrence of Mn^{4+} ions in the grown films with the typical octahedral environment. Similar results were found in the measurements of the O K edge of these compounds (see Figure 16b). At this edge, significant differences are found between Mn^{3+} and Mn^{4+} standards. The XAS spectrum of $CaMnO_3$ shows huge pre-peak structures ascribed to strong hybridization between O *2p*- and Mn *3d*-states.[45,46] Similar pre-peaks are observed in the spectrum of $Sr_{0.5}Ba_{0.5}MnO_3$ film supporting the existence of a similar Mn^{4+} ion in both compounds.

CONCLUSIONS

We have thoroughly investigated the stability of the perovskite phase over the more stable hexagonal phase in solid solution $(Sr_{1-x}Ba_x)MnO_3$ in thin films. For the first time we demonstrate, through epitaxial stabilization, the feasibility of growing the pseudocubic phase in thin films up to 50% of Ba-content. The perovskite phase was only achieved in a narrow window of experimental conditions, which worsens on increasing the Ba-content by forcing the use of increasingly lower partial oxygen pressures during growth. This fact was related to the perovskite tolerance factor, in which the formation during deposition of sufficiently larger Mn^{3+}

cations substituting smaller Mn^{4+} ions was required to compensate large Ba^{2+} cations. Additionally, we have found that tensile strain favors the pseudocubic phase formation of $(Sr_{1-x}Ba_x)MnO_3$ compounds, whereas compressive strain hinders its stability. By in-situ slowly cooling down the films in a pure oxygen atmosphere after growth the presence of Mn^{4+} was found to be majority in $(Sr_{1-x}Ba_x)MnO_3$ films. Due to the poor stability of the perovskite phase, pure pseudocubic films can only be obtained up to a certain thickness limit –which decreases upon Ba-doping– above which the formation of twin domains and the presence of hexagonal regions appear. Epitaxial perovskite $(Sr_{1-x}Ba_x)MnO_3$ thin films were found to grow completely strained over a wide range of tensile-straining substrates, which provides access to novel phases absent in bulk specimens. Thus, we demonstrate the possibility to modify the structure at will of potential magnetoelectric multiferroic $(Sr,Ba)MnO_3$ system either by strain engineering or by chemical pressure (Ba-content). Because of the intimate relation in this system between structure and properties such as ferroic transition temperatures, polar phases, magnetic ground states or magnetoelectric coupling, our finding might stimulate further research on novel functionalities in strained $(Sr_{1-x}Ba_x)MnO_3$ thin films.

ASSOCIATED CONTENT

Supporting Information. XRD and structure data of stoichiometric polycrystalline $(Sr_{1-x}Ba_x)MnO_3$ ceramics PLD targets with single-phase hexagonal 4H structure. This material is available free of charge via the Internet at http://pubs.acs.org.

AUTHOR INFORMATION

Corresponding Author

*E-mail: eric.langenberg.perez@gmail.com

Present Addresses

† Centro de Investigación en Química Biolóxica e Materiais Moleculares (CIQUS), Universidade de Santiago de Compostela, 15782 Santiago de Compostela, Spain.

Author Contributions

The manuscript was written through contributions of all authors. All authors have given approval to the final version of the manuscript.

Notes

The authors declare no competing financial interest.

ACKNOWLEDGMENT

This work was supported by the Spanish Ministry of Economy and Competitiveness through projects MAT2012-38213-C02-01 and MAT2014-51982-C2 including FEDER funding, by the Aragón Regional Government through projects E26 and CTPP4/11 and by the European Union under the Seventh Framework Programme under a contract for an Integrated Infrastructure Initiative Reference 312483-ESTEEM2.

REFERENCES

(1) Wang, K. F.; Liu, J. –M.; Ren, Z. F. Multiferroicity: the Coupling between Magnetic and Polarization Orders. *Adv. Phys.* **2009**, *58*, 321–448.

(2) Martin, L. W.; Chu, Y. –H.; Ramesh, R. Advances in the Growth and Characterization of Magnetic, Ferroelectric, and Multiferroic Oxide Thin Films. *Mater. Sci. Eng. R* **2010**, *68*, 89–133.

(3) Izyumskaya, N.; Alivov, Ya.; Morkoç, H. Oxides, Oxides, and more Oxides: High-K Oxides, Ferroelectrics, Ferromagnetics, and Multiferroics. *Crit. Rev. Solid State Mater. Sci.* **2009**, *34*, 89–179.

(4) Rao, C. N. R.; Sundaresan, A.; Saha, R. Multiferroic and Magnetoelectric Oxides: The Emerging Scenario. *J. Phys. Chem. Lett.* **2012**, *3*, 2237–2246.

(5) Cohen, R. E. Origin of Ferroelectricity in Perovskite Oxides. *Nature (London, U.K.)* **1992**, *358*, 136–138.

(6) Hill, N. A. Why Are There so Few Magnetic Ferroelectrics? *J. Phys. Chem. B* **2000**, *104*, 6694–6709.

(7) van den Brink, J.; Khomskii, D. I. Multiferroicity Due to Charge Ordering. *J. Phys.: Condens. Matter* **2008**, *20*, 434217 (12 pp.).

(8) van Aken, B. B.; Palstra, T. T. M.; Filippetti, A.; Spaldin, N. A. The Origin of Ferroelectricity in Magnetoelectric $YMnO_3$. *Nat. Mater.* **2004**, *3*, 164–170.

(9) Seshadri, R.; Hill, N. A. Visualizing the Role of Bi 6s "Lone Pairs" in the Off-Center Distortion in Ferromagnetic $BiMnO_3$. *Chem. Mater.* **2001**, *13*, 2892–2899.

(10) Langenberg, E.; Fina, I.; Gemeiner, P.; Dkhil, B.; Fàbrega, L.; Varela, M.; Fontcuberta, J. Ferroelectric Phase Transition in Strained Multiferroic $(Bi_{0.9}La_{0.1})_2NiMnO_6$ Thin Films. *Appl. Phys. Lett.* **2012**, *100*, 022902 (3 pp.).

(11) Kimura, T.; Lawes, G.; Goto, T.; Tokura, Y.; Ramirez, A. P. Magnetoelectric Phase Diagrams of Orthorhombic $RMnO_3$ (R = Gd, Tb, and Dy). *Phys. Rev. B: Condens. Matter Mater. Phys.* **2005**, *71*, 224425 (13 pp.).

(12) Rondinelli, J. M.; Eidelson, A. S.; Spaldin, N. A. Non-d^0 Mn-Driven Ferroelectricity in Antiferromagnetic $BaMnO_3$. *Phys. Rev. B: Condens. Matter Mater. Phys.* **2009**, *79*, 205119 (6 pp.).

(13) Bhattacharjee, S.; Bousquet, E.; Ghosez, P. Engineering Multiferroism in $CaMnO_3$. *Phys. Rev. Lett.* **2009**, *102*, 117602 (4 pp.).

(14) Lee, J. H.; Rabe, K. M. Epitaxial-Strain-Induced Multiferroicity in $SrMnO_3$ from First Principles. *Phys. Rev. Lett.* **2010**, *104*, 207204 (4 pp.).

(15) Hong, J.; Stroppa, A.; Íñiguez, J.; Picozzi, S.; Vanderbilt, D. Spin-Phonon Coupling Effects in Transition-Metal Perovskites: A DFT + U and Hybrid-Functional Study. *Phys. Rev. B: Condens. Matter Mater. Phys.* **2012**, *85*, 054417 (12 pp.).

(16) Sakai, H.; Fujioka, J.; Fukuda, T.; Okuyama, D.; Hashizume, D.; Kagawa, F.; Nakao, H.; Murakami, Y.; Arima, T.; Baron, A. Q. R.; Taguchi, Y.; Tokura, Y. Displacement-Type Ferroelectricity with Off-Center Magnetic Ions in Perovskite $Sr_{1-x}Ba_xMnO_3$. *Phys. Rev. Lett.* **2011**, *107*, 137601 (4 pp.).

(17) Pratt, D. K.; Lynn, J. W.; Mais, J.; Chmaissem, O.; Brown, D. E.; Kolesnik, S.; Dabrowski, B. Neutron Scattering Studies of the Ferroelectric Distortion and Spin Dynamics in the Type-1 Multiferroic Perovskite $Sr_{0.56}Ba_{0.44}MnO_3$. *Phys. Rev. B: Condens. Matter Mater. Phys.* **2014**, *90*, 140401(R) (5 pp.).

(18) Chmaissem, O.; Dabrovski, B.; Kolesnik, S.; Mais, J.; Brown, D. E.; Kruk, R.; Prior, P.; Pyles, B.; Jorgensen, J. D. Relationship between Structural Parameters and the Néel Temperature

in $Sr_{1-x}Ca_xMnO_3$ ($0 < \sim x < \sim 1$) and $Sr_{1-y}Ba_yMnO_3$ ($y < \sim 0.2$). *Phys. Rev. B: Condens. Matter Mater. Phys.* **2001**, *64*, 134412 (9 pp.).

(19) Giovannetti, G.; Kumar, S.; Ortix, C.; Capone, M.; van den Brink, J. Microscopic Origin of Large Negative Magnetoelectric Coupling in $Sr_{1/2}Ba_{1/2}MnO_3$. *Phys. Rev. Lett.* **2012**, *109*, 107601 (5 pp).

(20) Sakai, H.; Fujioka, J.; Fukuda, T.; Bahramy, M. S.; Okuyama, D.; Arita, R.; Arima, T.; Baron, A. Q. R.; Taguchi, Y.; Tokura, Y. Soft Phonon Mode Coupled with Antiferromagnetic Order Incipient-Ferroelectric Mott Insulators $Sr_{1-x}Ba_xMnO_3$. *Phys. Rev. B: Condens. Matter Mater. Phys.* **2012**, *86*, 104407 (11 pp).

(21) Glinchuk, M. D.; Eliseev, E. A.; Gu, Y.; Chen, L. –Q.; Gopalan, V.; Morozovska, A. N. Electric-Field Induced Ferromagnetic Phase in Paraelectric Antiferromagnets. *Phys. Rev. B: Condens. Matter Mater. Phys.* **2014**, *89*, 014112 (6 pp).

(22) Negas, T. The $Ba_{1-y}Sr_yMnO_{3-x}$ System. *J. Solid State Chem.* **1973**, *6*, 136–150.

(23) Dabrowski, B.; Chmaissem, O.; Mais, J.; Kolesnik, S.; Jorgensen, J. D.; Short, S. Tolerance Factor Rules for $Sr_{1-x-y}Ca_xBa_yMnO_3$ Perovskites. *J. Solid State Chem.* **2003**, *170*, 154–164.

(24) Balakirev, V. F.; Golikov, Y. V. Phase Relations in Alkaline Earth-Manganese-Oxygen Systems: Equilibrium and Metastable States. *Inorg. Mater.* **2006**, *42*, S49–S69.

(25) Adkin, J. J.; Hayward, M. A. $BaMnO_{3-x}$ Revisited: A Structural and Magnetic Study. *Chem. Mater.* **2007**, *19*, 755–762.

(26) Schlom, D. G.; Chen, L. -Q.; Fennie, C. J.; Gopalan, V.; Muller, D. A.; Pan, X.; Ramesh, R.; Uecker, R. Elastic Strain Engineering of Ferroic Oxides. *MRS Bull.* **2014**, *39*, 118–130.

(27) Becher, C.; Maurel, L.; Aschauer, U.; Lilienblum, M.; Magén, C.; Meier, D.; Langenberg, E.; Trassin, M.; Blasco, J. Krug, I. P.; Algarabel, P. A.; Spaldin, N. A.; Pardo, J. A.; Fiebig, M. Strain-Induced Coupling of Electrical Polarization and Structural Defects in $SrMnO_3$ Films. *Nat. Nanotechnol.* **2015**, *10*, 661–665.

(28) Gorbenko, O. Y.; Samoilenkov, S. V.; Graboy, I. E.; Kaul, A. R. Epitaxial Stabilization of Oxides in Thin Films. *Chem. Mater.* **2002**, *14*, 4026–4043.

(29) Novojilov, M. A.; Gorbenko, O. Y.; Graboy, I. E.; Kaul, A. R.; Zandbergen, H. W.; Babushkina, N. A.; Belova, L. M. Perovskite Rare-earth Nickelates in the Thin-film Epitaxial State. *Appl. Phys. Lett.* **2000**, *76*, 2041–2043.

(30) Lee, J.-H.; Murugavel, P.; Ryu, H.; Lee, D.; Jo, J. Y.; Kim, J. W.; Kim, H. J.; Kim, K. H.; Jo, Y.; Jung, M.-H.; Oh, Y. H.; Kim, Y.-H.; Yoon, J.-G.; Chung, J.-S.; Noh, T. W. Epitaxial Stabilization of a New Multiferroic Hexagonal Phase of $TbMnO_3$ Thin Films. *Adv. Mater.* **2006**, *18*, 3125–3129.

(31) Martí, X.; Sánchez, F. Skumryev, V.; Laukhin, V.; Ferrater, C.; García-Cuenca, M. V.; Varela, M.; Fontcuberta, J. Crystal Texture Selection in Epitaxies of Orthorhombic Antiferromagnetic $YMnO_3$ films. *Thin Solid Films* **2008**, *516*, 4899–4907.

(32) $YAlO_3$ and Rare-earth scandate substrates used in this work, namely $DyScO_3$, $TbScO_3$, $GdScO_3$, are actually orthorhombic and (110)-oriented. Still, with this orientation the orthorhombic structure can be described as a distorted pseudocubic structure, in which the new

pseudocubic in-plane lattice parametes are obtained computing $a_{pc} = \frac{1}{2}\sqrt{a_o^2 + b_o^2}$; $b_{pc} = \frac{1}{2}c_o$, where "pc" and "o" subscripts denote pseudocubic and orthorhombic, respectively. For the sake of simplicity in this work we have used the pseudocubic notation with an average pseudocubic lattice parameter. Note that despite $a_{pc} \neq b_{pc}$, their values are very similar. See, for instance, reference 33.

(33) Uecker, R.; Velickov, B.; Klimm, D.; Bertram, R.; Bernhagen, M.; Rabe, M.; Albrecht, M.; Fornari, R.; Schlom, D. G. Properties of Rare-Earth Scandate Single Crystals (Re = Nd-Dy). *J. Cryst. Growth* **2008**, *310*, 2649–2658.

(34) Choi, K. J.; Biegalski, M.; Li, Y. L.; Sharan, A.; Schubert, J.; Uecker, R.; Reiche, P.; Chen, Y. B.; Pan, X. Q.; Gopalan, V.; Chen, L. -Q.; Schlom, D. G.; Eom, C. B. Enhancement of Ferroelectricity in Strained $BaTiO_3$ Thin Films. *Science* **2004**, *306*, 1005–1009.

(35) Adamo, C.; Ke, X.; Schiffer, P.; Soukiassian, A.; Warusawithana, M.; Maritato, L.; Schlom, D. G. Electrical and Magnetic Properties of $(SrMnO_3)_n(LaMnO_3)_{2n}$ Superlattices. *Appl. Phys. Lett.* **2008**, *92*, 112508 (3 pp.).

(36) Saïb, M.; Belmeguenai, M.; Méchin, L.; Bloyet, D.; Flament, S. Magnetization Reversal in Patterned $La_{0.67}Sr_{0.33}MnO_3$ Thin Films by Magneto-Optical Kerr Imaging. *J. Appl. Phys.* **2008**, *103*, 113905 (5 pp.).

(37) Kan, D.; Aso, R.; Kurata, H.; Shimakawa, Y. Thickness-Dependent Structure-Property Relationships in Strained (110) $SrRuO_3$ Thin Films. *Adv. Funct. Mater.* **2013**, *23*, 1129–1136.

(38) Shannon, R. D. Revised Effective Ionic Radii and Systematic Studies of Interatomic Distances in Halides and Chalcogenides. *Acta Crystallogr*. **1976**, *A32*, 751–767.

(39) Müller, P.; Störmer, H.; Meffert, M.; Dieterle, L.; Niedrig, C.; Wagner, S. F.; Ivers-Tiffée, E.; Gerthsen, D. Secondary Phase Formation in $Ba_{0.5}Sr_{0.5}Co_{0.8}Fe_{0.2}O_{3-d}$ Studied by Electron Microscopy. *Chem. Mater.* **2013**, *25*, 564–573.

(40) For better accuracy, out-of-plane lattice parameter of $(Sr_{1-x}Ba_x)MnO_3$ films were computed from the 2θ position of the (002) reflection in θ/2θ XRD diffractograms.

(41) Ranno, L; Llobet, A.; Tiron, R.; Favre-Nicolin, E. Strain-Induced Magnetic Anisotropy in Epitaxial Manganite Films. *Appl. Surf. Sci.* **2002**, *188*, 170–175.

(42) Infante, I. C.; Sánchez, F.; Fontcuberta, J.; Wojcik, M.; Jedryka, E.; Estradé, S.; Peiró, F.; Arbiol, J.; Laukhin, V.; Espinós, J. P. Elastic and Orbital Effects on Thickness-Dependent Properties of Manganite Thin Films. *Phys. Rev. B: Condens. Matter Mater. Phys.* **2007**, *76*, 224415 (12 pp.).

(43) Adamo, C.; Ke, X.; Wang, H. Q.; Xin, H. L.; Heeg, T.; Hawley, M. E.; Zander, W.; Schubert, J.; Schiffer, P.; Muller, D. A.; Maritano, L.; Schlom, D. G. Effect of Biaxial Strain on the Electrical and Magnetic Properties of (001) $La_{0.7}Sr_{0.3}MnO_3$ Thin Films. *Appl. Phys. Lett.* **2009**, *95*, 112504 (3 pp.).

(44) Aschauer, U.; Pfenninger, R.; Selbach, S. M.; Grande, T.; Spaldin, N. A. Strain-Controlled Oxygen Vacancy Formation and Ordering in $CaMnO_3$. *Phys. Rev. B: Condens. Matter Mater. Phys.* **2013**, *88*, 054111 (7 pp.).

(45) Subías, G; García, J; Sánchez, M. C.; Blasco, J.; Proietti, M. G. Soft X-Ray Absorption Spectroscopy (Mn $L_{2,3}$ and O K) in Mixed Valence Manganites. *Surf. Rev. Lett.* **2002**, *9*, 1071–1078.

(46) Kurata, H.; Colliex, C. Electron-Energy-Loss Core-Edge Structures in Manganese Oxides. *Phys. Rev. B: Condens. Matter Mater. Phys.* **1993**, *48*, 2102–2108.

FIGURES

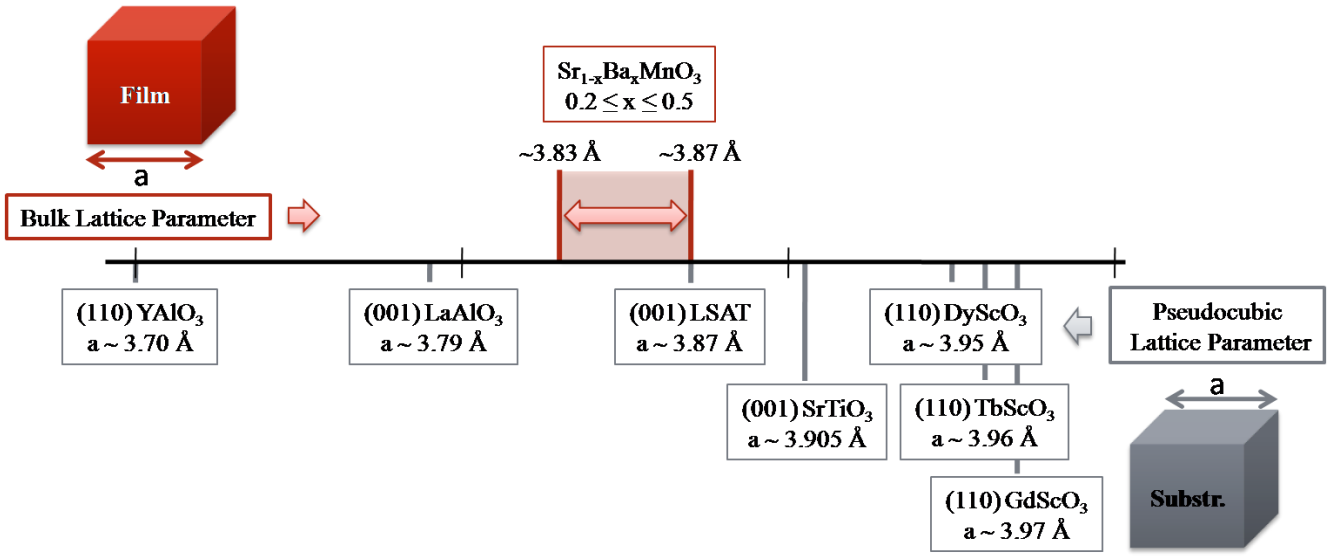

Figure 1. Sketch showing the pseudocubic lattice parameters of the substrates used in this work as well as the bulk lattice parameters of $(Sr_{1-x}Ba_x)MnO_3$ $(0.2 \leq x \leq 0.5)$ computed from Ref. 16.

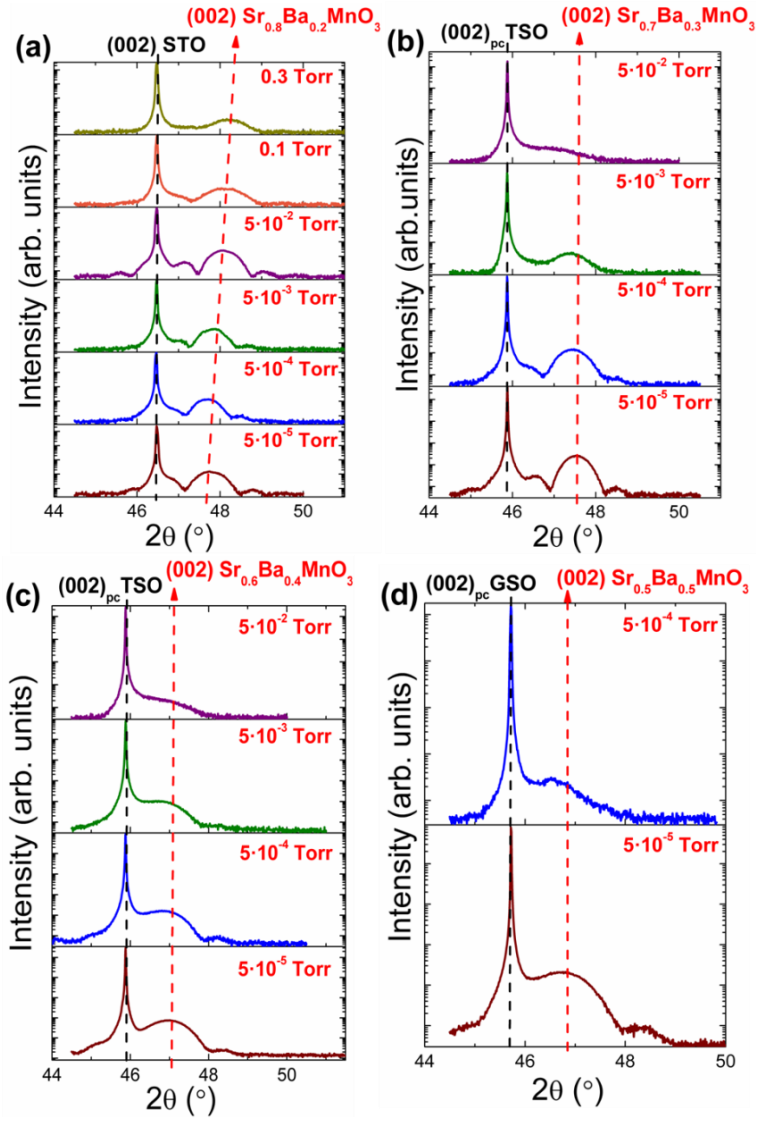

Figure 2. θ/2θ XRD patterns around (002) pseudocubic reflection of $(Sr_{1-x}Ba_x)MnO_3$ films grown at 1000°C and at different oxygen pressures on selected substrates. **(a)** x = 0.2, 14 nm of thickness, on STO substrates; **(b)** x = 0.3, 17 nm of thickness, on TSO substrates; **(c)** x = 0.4, 12 nm of thickness, on TSO substrates; **(d)** x = 0.5, 9 nm of thickness, on GSO substrates. Black and red dotted line denote the (002) pseudocubic reflection of substrate and film, respectively.

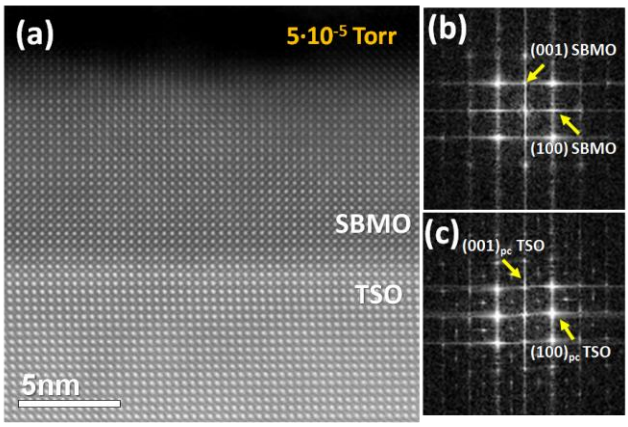

Figure 3. (a) HAADF-STEM image of [100] cross section of $(Sr_{0.6}Ba_{0.4})MnO_3$ (SBMO) films grown on TSO at $5 \cdot 10^{-5}$ Torr. Fast Fourier Transform of **(b)** film and **(c)** substrate. "pc" subscript denotes pseudocubic reflection.

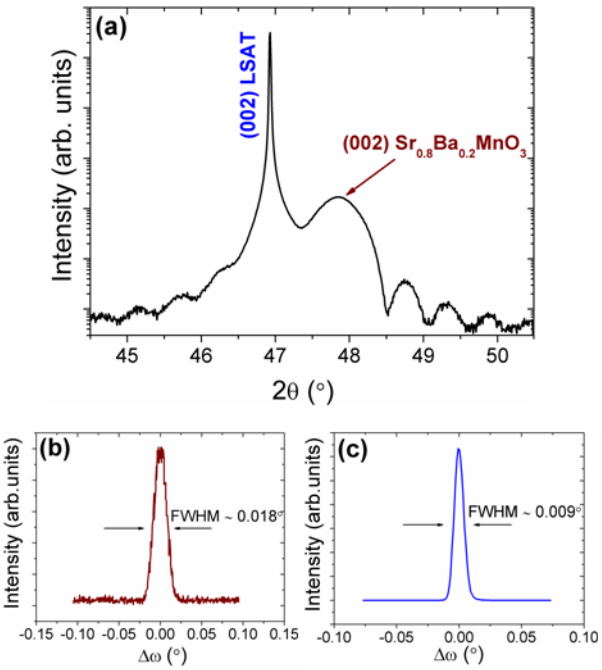

Figure 4. (a) θ/2θ XRD pattern of 20-nm $Sr_{0.8}Ba_{0.2}MnO_3$ film grown on LSAT. Corresponding XRD rocking curve around the (002) reflection of **(b)** $Sr_{0.8}Ba_{0.2}MnO_3$ film and **(c)** LSAT substrate.

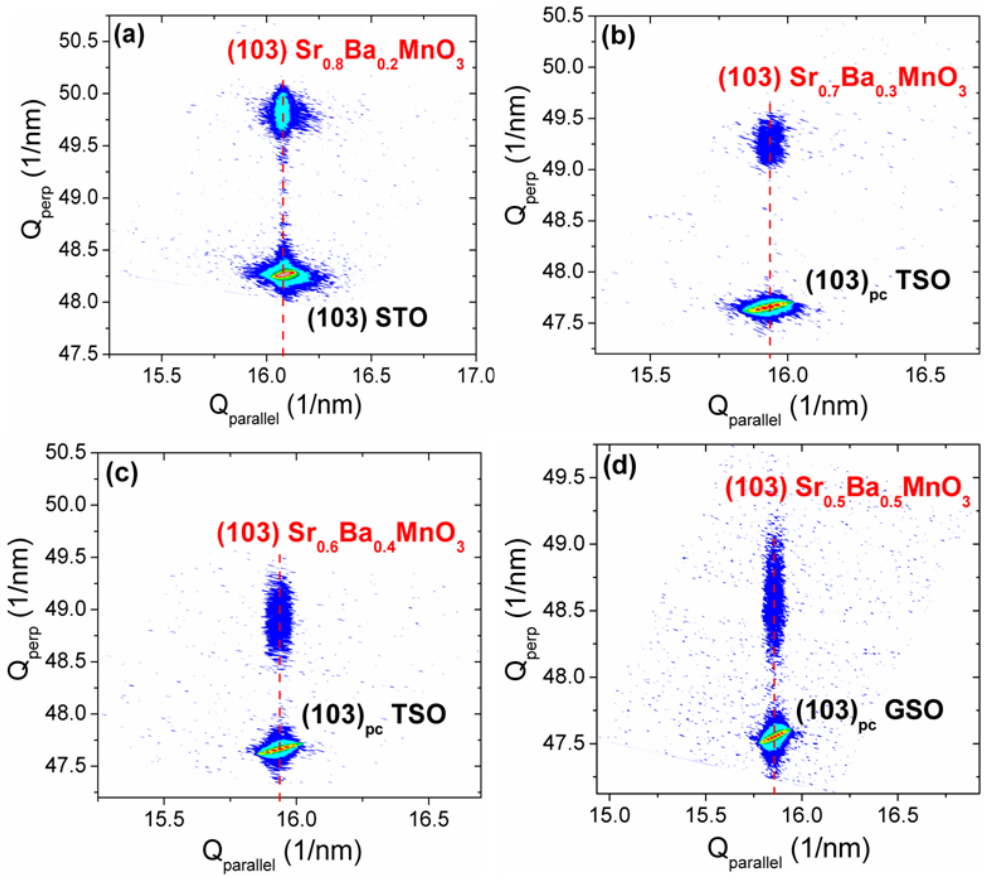

Figure 5. Reciprocal space maps around the pseudocubic (103) reflection of $(Sr_{1-x}Ba_x)MnO_3$ thin films: **(a)** 22-nm $Sr_{0.8}Ba_{0.2}MnO_3$ on STO, **(b)** 16-nm $Sr_{0.7}Ba_{0.3}MnO_3$ on TSO, **(c)** 11-nm $Sr_{0.6}Ba_{0.4}MnO_3$ on TSO, **(d)** 9-nm $Sr_{0.5}Ba_{0.5}MnO_3$ on GSO, where "pc" subscript denotes pseudocubic reflection. Red dashed line indicates the in-plane lattice parameter being coincident with that of the substrate.

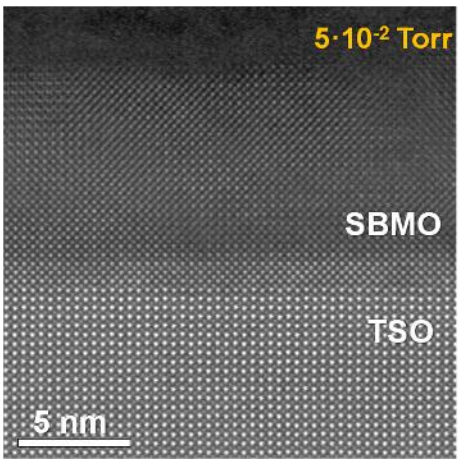

Figure 6. HAADF-STEM image of [100] cross section of $(Sr_{0.6}Ba_{0.4})MnO_3$ (SBMO) film grown on TSO at $5 \cdot 10^{-2}$ Torr.

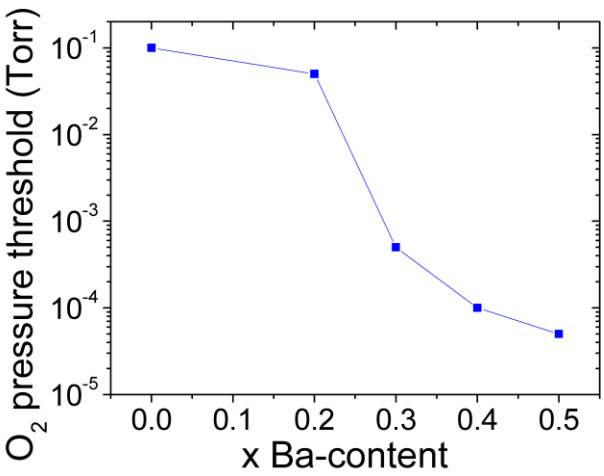

Figure 7. Ba-dependency of the oxygen pressure threshold during growth, below which the pseudocubic phase is fully stabilized in $(Sr_{1-x}Ba_x)MnO_3$ films.

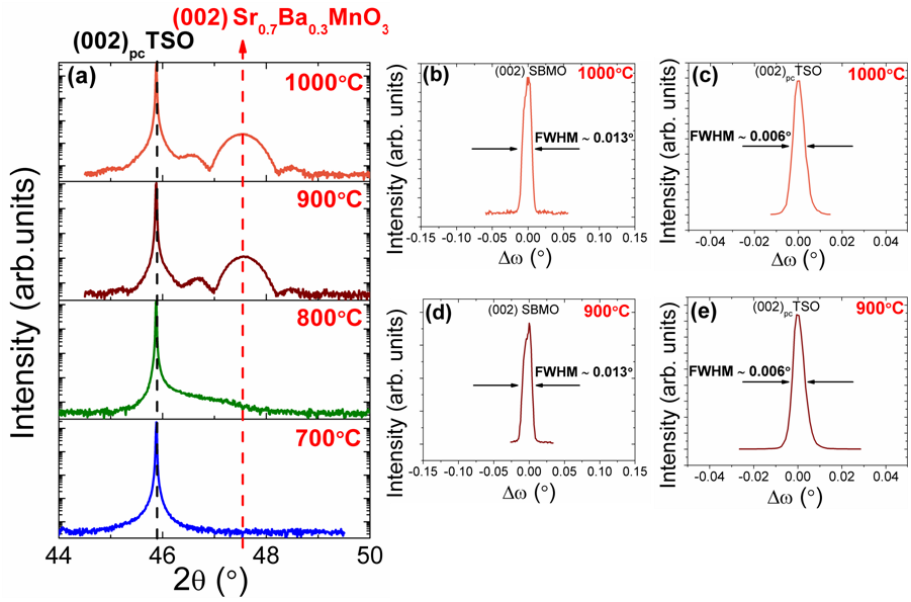

Figure 8. (a) θ/2θ XRD patterns around (002) pseudocubic reflection of 15-nm thick $(Sr_{0.7}Ba_{0.3})MnO_3$ films grown at different temperatures and $5 \cdot 10^{-5}$ Torr O_2 pressure on TSO substrates. Black and red dotted line denote the (002) pseudocubic reflection of substrate and film, respectively. **(b)** and **(c)** XRD rocking curves of (002) reflection of $(Sr_{0.7}Ba_{0.3})MnO_3$ film and TSO substrate, respectively, for the film grown at 1000°C. **(d)** and **(e)** XRD rocking curves of (002) reflection of $(Sr_{0.7}Ba_{0.3})MnO_3$ film and TSO substrate, respectively, for the film grown at 900°C.

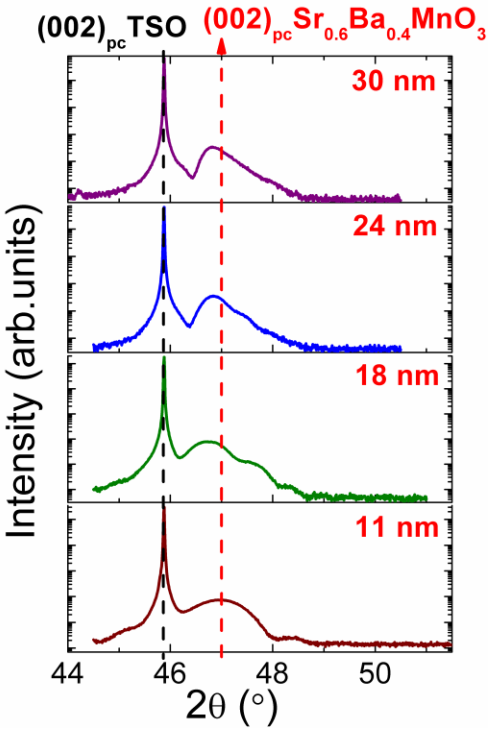

Figure 9. Thickness dependence of the perovskite phase: θ/2θ XRD patterns around (002) pseudocubic reflection of $(Sr_{0.6}Ba_{0.4})MnO_3$ films grown on TSO.

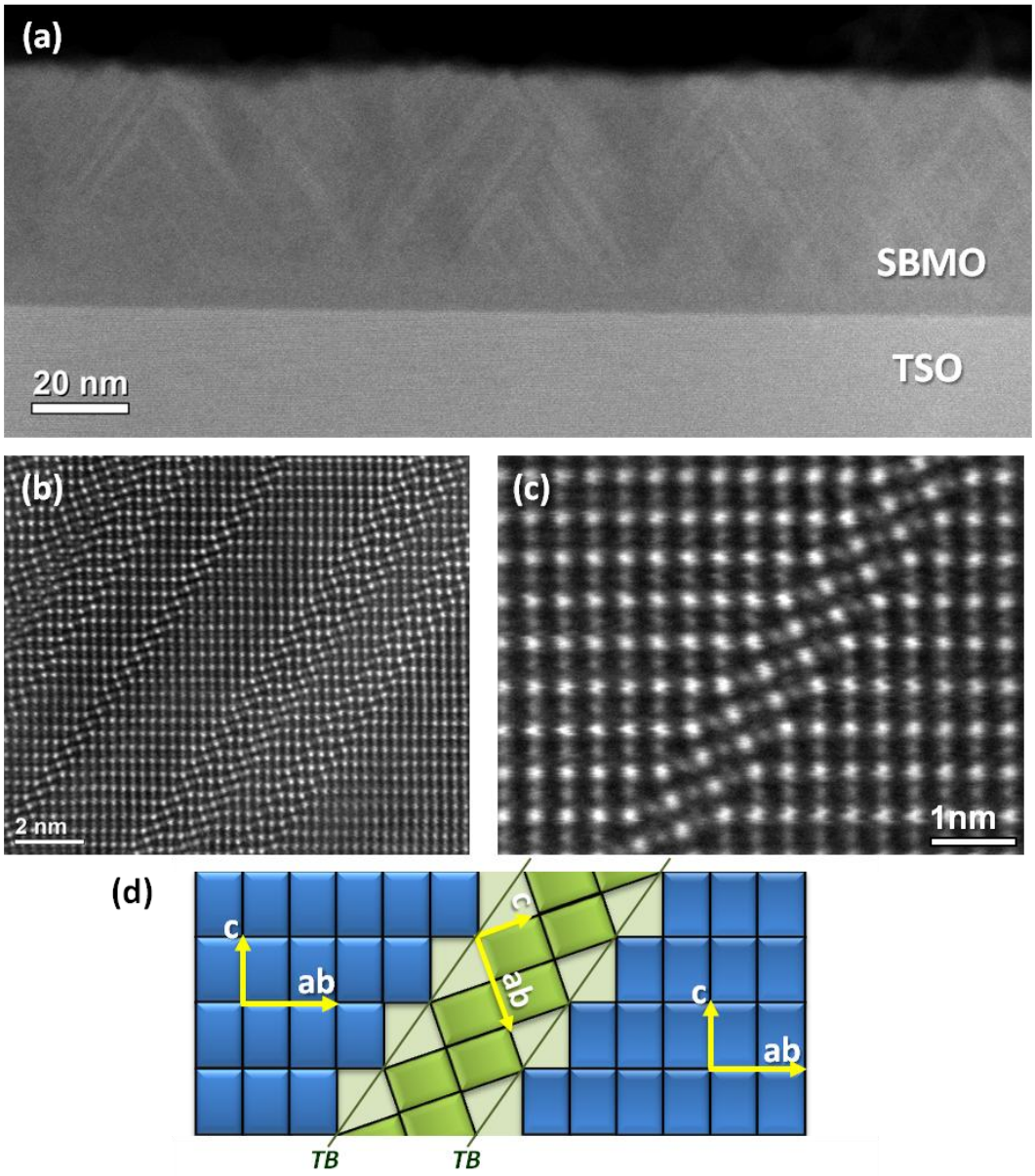

Figure 10. HAADF-STEM image of [110] cross section of 50-nm $(Sr_{0.6}Ba_{0.4})MnO_3$ (SBMO) thin film grown on TSO. **(a)** Low-magnification image. **(b)** and **(c)** High-magnification images showing the twin domain system. **(d)** Sketch showing the epitaxially-oriented (blue) and the misoriented (green) twin domains.

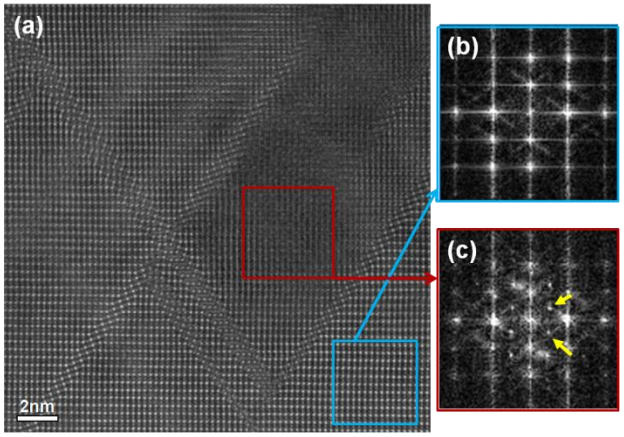

Figure 11. (a) HAADF-STEM image of [110] cross section of 50-nm $(Sr_{0.6}Ba_{0.4})MnO_3$ thin film grown on TSO. **(b)** and **(c)** FFT of the highlighted regions corresponding to the pseudocubic and hexagonal phase, respectively.

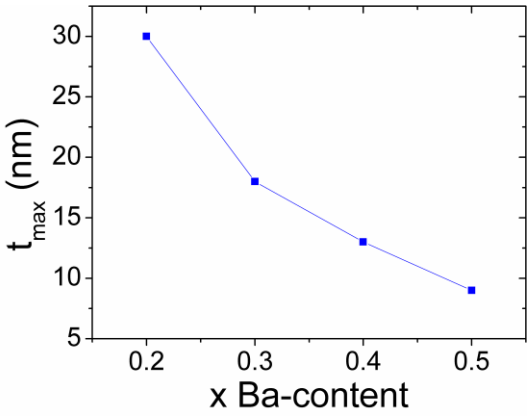

Figure 12. Ba-content dependence of the critical thickness, t_{max}, below which the perovskite phase is completely stabilized.

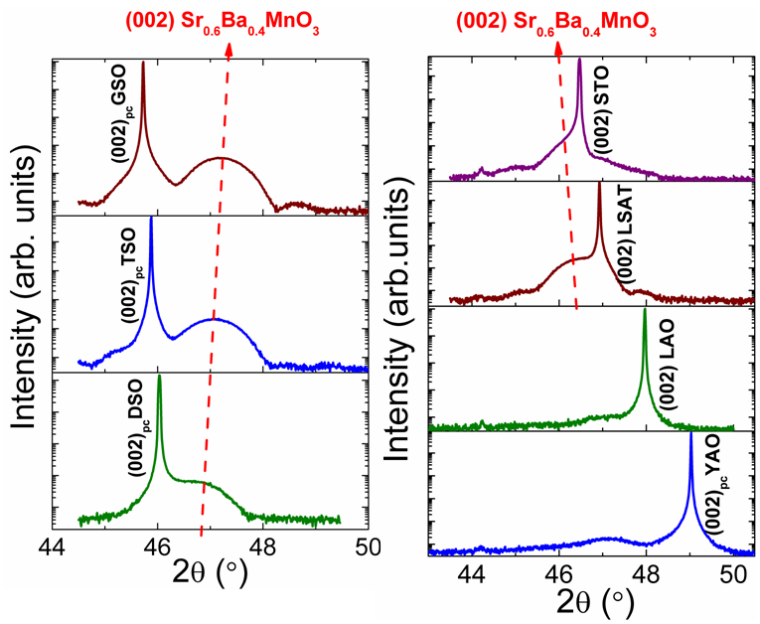

Figure 13. Strain dependence of the perovskite phase: θ/2θ XRD patterns around (002) pseudocubic reflection of $(Sr_{0.6}Ba_{0.4})MnO_3$ films grown on $(001)_{pc}$-oriented substrates[26] (indicated in the respective plots).

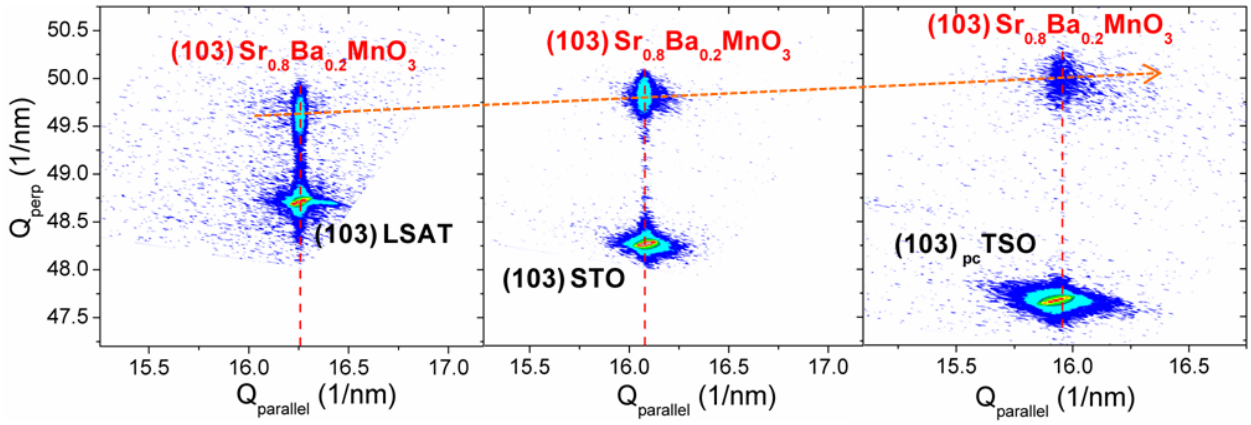

Figure 14. Reciprocal space maps around the pseudocubic (103) reflection of $(Sr_{0.8}Ba_{0.2})MnO_3$ thin films grown on LSAT, STO and TSO. Red and orange dotted lines indicate the in-plane lattice parameter being coincident with that of the substrate and the out-of-plane lattice parameter being decreased upon tensile strain, respectively.

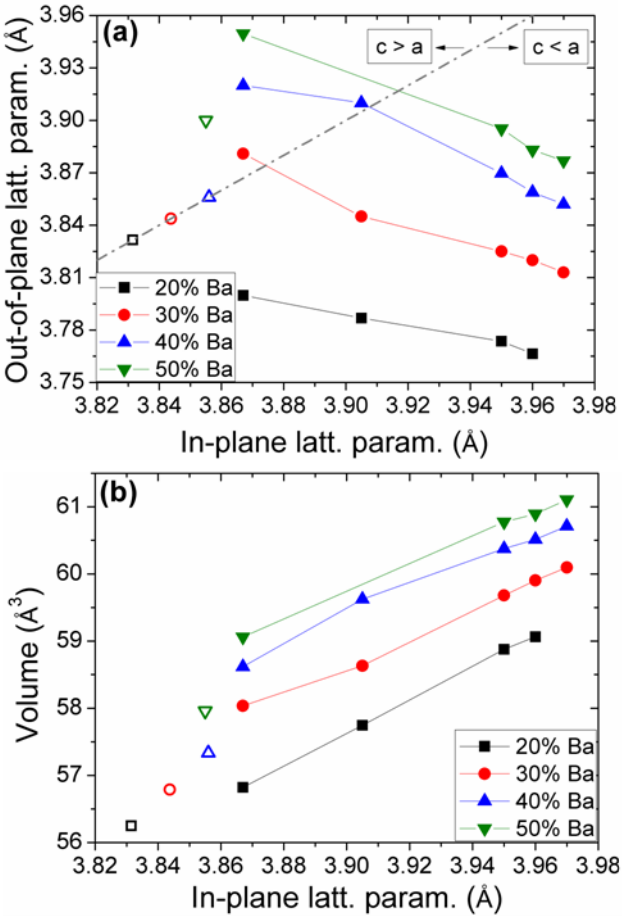

Figure 15. Structure of strained pseudocubic $(Sr_{1-x}Ba_x)MnO_3$ thin films. Black square, red circle, blue up triangle and green down triangle symbols denote 20%, 30%, 40% and 50% Ba-doping, respectively. Corresponding open symbols denote bulk values computed from Ref. 16. **(a)** Out-of-plane lattice parameter – *c* – vs in-plane lattice parameter fixed by the substrate – *a* –. Dash-dotted line separates the region where $c > a$ and $c < a$. **(b)** Unit cell volume as a function of in-plane lattice parameter.

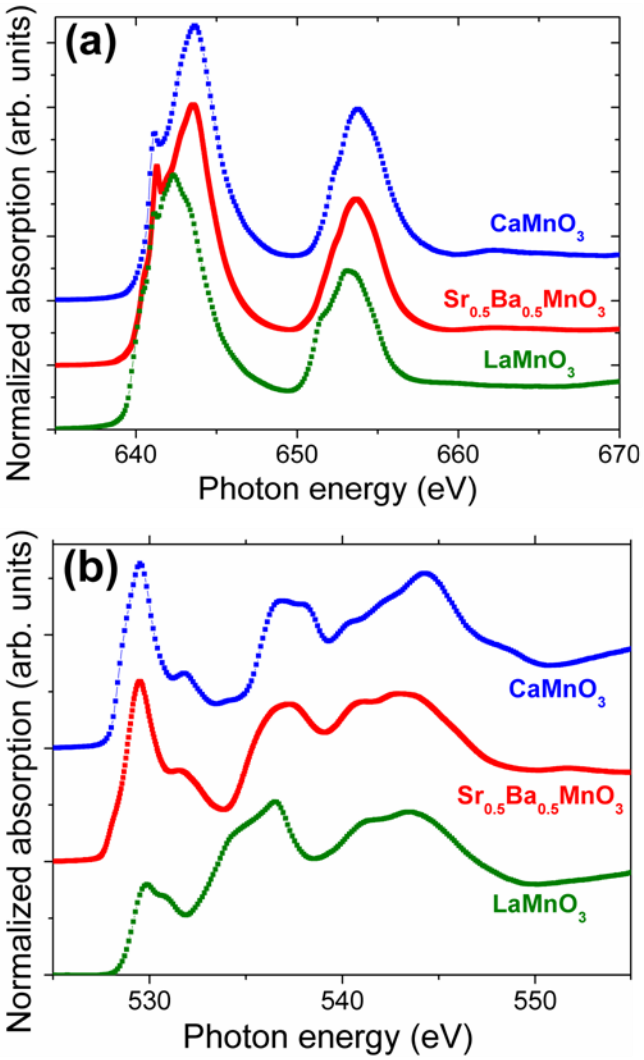

Figure 16. (a) Mn $L_{2,3}$ and **(b)** O K XAS spectra at room temperature of $Sr_{0.5}Ba_{0.5}MnO_3$ thin film grown on GSO. We have included $CaMnO_3$* and $LaMnO_3$* reference samples. *Data taken from Ref. 44.

GRAPHIC FOR MANUSCRIPT/ TOC GRAPHIC